Oxygen carrier aided combustion (OCAC) of two waste fuels - Experimental and theoretical study of the interaction between ilmenite and

(article starts on next page)

Check for
updates

Oxygen carrier aided combustion (OCAC) of two waste fuels - Experimental and theoretical study of the interaction between ilmenite and zinc, copper and lead

Ivana Staničić [a],[*], Tobias Mattisson [a], Rainer Backman [b], Yu Cao [c], Magnus Rydén [a]

[a] *Department of Space, Earth and Environment, Division of Energy Technology, Chalmers University of Technology, SE-412 96, Gothenburg, Sweden*
[b] *Department of Applied Physics and Electronics, Thermochemical Energy Conversion Laboratory, Umeå University, SE 901 87, Umeå, Sweden*
[c] *Department of Industrial and Materials Science, Chalmers University of Technology, SE-412 96, Gothenburg, Sweden*

ABSTRACT

Zinc, copper and lead are amongst the more abundant trace metals in waste fuels such as municipal solid waste and recovered waste wood. The ashes from waste fuels could contain high contents of these metals, which could be valuable but also toxic in certain environments. Oxygen carrier aided combustion, OCAC, is a novel technology for combustion of biomass and waste. Utilizing oxygen carriers could affect the fate of these metals and have implications for stability and recycling.

The aim of this work is to study the fate of zinc, copper and lead during oxygen carrier aided combustion of two waste fuels utilizing ilmenite as an oxygen carrier. In total, four samples have been obtained from two different industrial fluidized bed boilers using ilmenite as bed material. Due to low concentrations, bulk analysis methods are not suitable for speciation, i.e. SEM/EDX and XRD. Hence, this investigation utilizes high resolution x-ray photoelectron spectroscopy (XPS), coupled to detailed thermodynamic modelling, with the aim of understanding trace metal speciation, distribution and phase composition.

Characterization of the four samples show that iron at the surface of ilmenite particles interact with both copper and zinc to form ferrites, $CuFe_2O_4$ and $ZnFe_2O_4$. Lead, on the other hand, is more prone to end up in the fly ash as condensed $PbCl_2$, but the mixed oxide $PbTiO_3$ could be identified at the oxygen carrier surface. Thermodynamic calculations were shown to be in line with the identified compounds.

1. Introduction

In order to limit the global average temperature increase to below 2 °C above pre-industrial levels as stated in the Paris agreement, greenhouse gas emissions need to be reduced to zero in less than twenty years [1]. This is a difficult task unless active removal of carbon dioxide (CO_2) from the atmosphere is enforced. The Nordic countries are world leading with respect to heat and power generation from sustainable biofuels. The location and available resources is well suited for development of Bio Energy with Carbon Capture and Storage (BECCS) [2]. To mitigate the greenhouse gas effect, one needs to consider energy sources beyond fossil fuels. Amongst these, biomass is one potentially sustainable option. It is therefore likely that the transition to renewable energy will result in an expansion of biomass resources [3,4]. On one hand the diverse nature enables biofuels to be utilized all over the world. On the other hand, this expansion leads to larger variation in both ash content and composition [5].

One technology which is capable of capturing carbon dioxide from combustion facilities is Chemical Looping Combustion (CLC) [6]. The technology is based on the use of metal oxides and their ability to be oxidized or reduced depending on the oxygen partial pressure of the surrounding gas. This way, combustion is carried out in two separate reactors without gas mixing between the two. The metal oxides are oxidized in the air reactor and transported to the fuel reactor where the fuel is oxidized using the oxygen supplied by the metal oxides. These metal oxides are referred to as oxygen carriers [7].

Another use for oxygen carriers is bed material for conventional combustion in circulating fluidized bed (CFB) boilers. This technology is referred to as Oxygen Carrier Aided Combustion (OCAC), see Fig. 1. OCAC is realized by replacing the commonly used bed material, such as

Fig. 1. Schematic description of Oxygen Carrier Aided Combustion (OCAC).

2. Background

The flexibility, efficiency and stability of CFB boilers is advantageous for biomass combustion. The ability to handle a wide range of fuels with different shapes and sizes allows for the use of heterogenous waste fuels such as municipal solid waste (MSW). However, these fuels also contain impurities. After a fuel has been combusted the remaining ash fraction will contain inorganic compounds. Both the amount and composition of ash varies widely depending on the source of the fuel. Biomass, for example, can contain an ash fraction between 0.1 and 40% [16]. The most common major (>1%) and minor (0.1–1%) elements in biomass ashes are Si, Ca, K, P, Al, Mg, Fe, S, Na and Mn [17]. Trace elements (<0.1%) commonly includes heavy metals such as Cd, Cu, Hg, Ni, Pb and Zn [17]. The chemistry of these elements in presence of oxygen carriers is unknown [18]. A complex chemistry can be expected with chemical transformation of metals in the gas-phase as well as interaction between bulk gas phase and ash components [19,20].

Problems which could arise with complex fuel compositions with respect to CLC and OCAC could be associated with deposition and corrosion problems, emissions of heavy metals, agglomeration of bed material and possibly other operation problems. Compared to forest fuels, waste fuels may have a varying composition with higher amounts of heavy metals and chlorides. Waste wood for example may contain elevated amounts of zinc, lead or copper if surface treated or impregnated but also higher amounts of chlorine compared to forest fuels [21]. Municipal solid waste is a complex heterogenous fuel. A typical analysis of MSW consist of food waste, PVC, cardboard, newspapers, wood waste, yard waste, shoes, leather, batteries, shredder waste etc. [22] Even though the total amount of trace elements may be relatively low they may cause unwanted effects in the boiler. For example, an enrichment of lead or zinc in the fly ash may cause it to become sticky and in worst case corrosive [23]. It may also lead to unwanted heavy metal emissions [24].

Zinc and lead are two of the more abundant metals in both recovered waste wood (RWW) and municipal solid waste (MSW). Copper is also one of the metals found in higher concentrations in MSW [25]. The fate of these elements under CLC and OCAC conditions is not known. If they end up in the ashes, and these are landfilled it will result in a loss of both monetary value and natural resources. Further, there may be a potential benefit if valuable metals are recovered or recycled which for example, could produce ashes with lower concentrations of heavy metals. Recovery and recycling may even become necessary as strict legislation of recycling targets, landfilling directives and waste handling are implemented by government agencies, such as the European Union. Thus, the chemistry between zinc, copper and lead and oxygen carriers need to be further understood.

2.1. Fate of trace elements

The fate of trace elements (TEs) have been commonly studied using thermodynamical equilibrium approaches [26–29]. However, some experimental studies have also been performed. For example, the release of TEs during waste combustion of wood, shoes, shredder waste and PVC has been studied by Pedersen et al. [30] where lab-scale release experiments were performed on dedicated waste fractions to predict trends and identify release mechanisms attributed to the specific waste fractions.

Dong et al. [31] studied the partitioning of heavy metals in MSW pyrolysis, gasification and incineration using lab-scale tubular furnace, fluidized bed reactors and thermodynamic calculations. Silica sand was used as bed material for the experiments. The study showed that reducing atmosphere has a positive effect on the evaporation of Cd, Zn and Pb while Cu, Ni and Cr were retained in bottom ash. Pb however becomes less volatile under fluidized bed conditions. This could be caused by incorporation reactions of metals with SiO_2 which is enhanced with increasing oxygen concentration as in equation (1) [31].
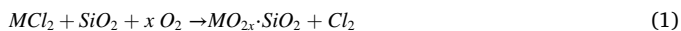
silica sand, with oxygen carriers. This setup has several advantages. The active bed material will be reduced in fuel rich parts and oxidized in oxygen rich parts leading to a more even oxygen availability and temperature in the boiler. Additionally, it can increase both combustion efficiency and capacity [8]. It has also been shown that this replacement reduces risk for agglomeration and has positive effects on emissions levels [9]. Since CFB boilers are used in industrial applications, OCAC can be a bridging technology towards CLC, and provide valuable insights on the performance of oxygen carriers and fuel. The OCAC-concept has been successfully operated in industrial application where ilmenite has been used as a bed material [10,11].

The main advantage with OCAC is that the technology can take advantage of existing CFB boilers. In Sweden there are 35 waste combustion facilities receiving around 6 million tons of waste yearly with high fractions of bio-based material such as wood and paper [12]. One of the dominating techniques used for energy recovery is fluidized beds which implies a great potential for OCAC globally. OCAC is especially suitable for biomass combustion as it has an ability to handle a wide range of biomass fuels. In recent years OCAC has been demonstrated at industrial scale, still the research around the technology is relatively limited [8,11] Biomass often contains significant amounts of moisture, volatiles and ash [5]. When burning highly volatile fuels the lateral mixing may be insufficient when using conventional bed material such as silica sand, resulting in a requirement of excess air. Although silica sand distributes the heat in the boiler the oxygen carriers also have the possibility to even out the oxygen distribution. This results in decreased amount of excess air required and increases the boiler efficiency. There are some studies conducted on the ash layer build-up and sulfur interaction when using ilmenite in OCAC-applications [13–15], but in general there is limited research conducted around this important technology, especially at industrial scale. Investigating samples obtained from industrial applications which utilize complex waste fuels can provide unique and highly relevant information on the solid-state chemistry and fate of important elements.

$$MCl_2 + SiO_2 + x\,O_2 \rightarrow MO_{2x}\!\cdot\!SiO_2 + Cl_2 \tag{1}$$

Under fluidized bed conditions the mixing is more intense and contact between feedstock and bed material is enhanced. The interaction with bed material forming compounds such as $Pb_3Ca_2Si_3O_{11}$ or $PbZnSiO_4$ could prevent Pb and Zn accumulating in the gas phase [31]. The metal-matrix reaction (1) is important as it affects the transfer of metals and is correlated to the presence of mineral substances, alkalis and the interactions among different existing metals. The study of Dong et al. summarized three main parameters affecting the partitioning of heavy metals under MSW thermal processes in the following points [31].

  i. The metal speciation; which is related to the redox atmosphere, temperature and presence of alkali, Cl, S and mineral substances.
  ii. The system characteristics, such as furnace type.
  iii. The mechanical entrainment of particles caused by gas velocity.

The bed material plays an important role in heavy metal partitioning. Silica sand is an inert material with respect to oxygen carrying capability. If an oxygen carrier is to be used additional reactions with TEs may be possible. Further, the oxygen partial pressure in CLC/OCAC may vary in a wide range, which could affect the chemistry.

TEs in fluidized bed combustion systems utilizing coal have been studied by Alvin et al. [32] using thermodynamic calculations as early as in 1977 with focus on lead, mercury, beryllium and fluorine. In 1994 Frandsen et al. [29] extensively investigated the equilibrium distribution of 18 TEs under both coal combustion and gasification conditions. While early research has focused on coal combustion more recent ones have investigated more complex fuels such as biomass and waste fuels. Studies have shown that combustion of waste derived fuels in fluidized bed boilers may result in increased amounts of TEs in the fly ashes besides the common alkali and alkaline earth metal compounds [33]. One important parameter is the availability of chlorine which couples the volatilization behavior of TEs with the chemistry of alkali metals and calcium which govern the availability of chlorine [33]. Thus, the condensation behavior and partitioning of TEs are important in these systems.

Enestam et al. [27] evaluated the condensation behavior of lead and zinc in BFB combustion of recovered waste wood. The study found that zinc and lead mainly vaporize as Zn(g) and Pb(g) in the reducing part of the furnace. Thus, condensation of metallic Pb, Zn and PbS can be expected in the lower reducing parts of the furnace if the temperature on the surface drops below the condensation temperature, while condensation of $PbCl_2$ and $ZnCl_2$ may be expected on the heat transfer surfaces later in the convection section.

A thermodynamic study performed by Becidan et al. [26] studied all the separate waste fractions of MSW and their influence on the behavior of alkali metals and TEs during combustion. MSW fractions having significant Na concentrations are constituents of the biogenic fraction of waste. When chlorine is available most of the Na forms NaCl. When Zn is added to the mixture it will mostly form ZnO(s) (during oxidizing conditions) since most of the chlorine is bounded as NaCl suppressing the formation of $ZnCl_2$. If most of the fuel consists of PVC (very small amount of Na) then $ZnCl_2$ will be the most thermodynamically stable compound. The same behavior is observed for lead which forms $PbCl_2$. When the sulfur and chlorine fraction is minor, Pb forms PbO(g). One common feature between the different MSW waste fractions is that lead is overwhelmingly found to be in the gas phase during combustion [26].

2.2. Interaction between biomass ash and oxygen carriers

A limited number of studies are available regarding the interaction between biomass ash and iron-based oxygen carriers [14,34–37]. Previous research on interactions between oxygen carriers and ash components has mainly focused on coal ashes and most of the studies are conducted in bench scale experiments [38–41]. For example, brown coal ash, rich in silica, iron and magnesium has been reported to react with both iron ore and ilmenite [42]. Gu, H et al. have investigated the interaction between iron ore and biomass ashes during CLC operation. Silica rich ashes were shown to produce molten potassium silicates which caused particle sintering and reactivity deterioration of the oxygen carrier. On the other hand, potassium rich ashes with relatively low amount of silica improved the reactivity during operation [35].

There are some studies available based on OCAC which have investigated the interaction between ilmenite and biomass ash [14,15]. The main interaction path has been reported to be with the major ash components calcium and potassium. Calcium forms a double ash layer on the ilmenite particle with increased iron content in between [15]. With increased time of exposure potassium diffuses into the ilmenite particle core forming titanates. Other observations relate to the segregation of iron to the surface and enrichment of titanium in the particle core [14,15,43]. Clearly, the chemistry of the main reactive ash components could be tightly connected to the fate of TEs, something which is investigated in this work.

2.3. Aim of study

The aim of this work is to study four industrial solid samples derived from OCAC of different waste fuels using the benchmark oxygen carrier ilmenite. Four ash samples will be characterized using experimental techniques, which will be compared to thermodynamic calculations.

More specifically, the objective is to study the interaction between the important trace elements copper, lead and zinc and the bed material, ilmenite. Further investigation of trace element behavior is of interest especially since no previous studies have focused on oxygen carrier interaction with trace elements. Due to low concentrations, bulk analysis methods are not suitable for speciation, i.e. SEM/EDX and XRD. Hence, this investigation utilizes high resolution x-ray photoelectron spectroscopy (XPS), coupled to detailed thermodynamic modelling, with the aim of improving understanding.

3. Method

There are several combined heat and power plants in Sweden that currently utilizes or have tested OCAC. This study will investigate the TE interaction with industrial bed samples extracted from plants located at Örtofta and Händelö, Sweden. Both plants utilize waste fuels and use ilmenite as bed material although in these specific cases the ilmenite was mixed with sand.

The plant at Örtofta consist of a 115 MW_{th} CFB boiler which supplies electricity and heat to the local district heating grid by burning biomass. The boiler is owned by the company Kraftringen. During operation around 60 ton of bed and biomass waste material is present in the system. Usually silica sand with an average particle size of 0.25 mm is used as a bed material. In this case however, Norwegian rock ilmenite was used. The biomass fuel consisted of a mixture of recovered waste wood and wood chips. The boiler operates at temperatures around 850 °C. Further information can be found elsewhere [8]. Two samples are analyzed from this plant. One contains higher fractions of ilmenite and the other one was sampled when silica sand was fed back to the boiler.

The plant at Händelö consists of a 75 MW_{th} CFB boiler which provides electricity and heat to the district heating network. The boiler is owned by the company E.ON. Since November 2014 the boiler has been operating regularly with ilmenite. The boiler normally operates with a mixture of MSW and industrial waste but allows sewage sludge and rubber to be used as well. The boiler temperature is kept above 850 °C. Further information can be found elsewhere [11,44]. From this plant one bottom ash and one fly ash sample are obtained for further analysis. During this time, the fuel consisted of a mixture of municipal solid waste and industrial waste.

3.1. Sample selection

Four industrial samples have been selected for investigation, presented in Table 1. All bottom ash samples have been sieved below <710 μm to remove larger pieces and magnetically separated two times to obtain an ilmenite rich fraction [43]. The magnetic separation was performed using a conveyor belt stretched across two horizontal cylinders. One cylinder constitutes of an electric motor while the other cylinder contains Rare Earth Roll (RER) magnets. The bed material was evenly fed to the belt using a distributor. The non-magnetic material follows a parabolic path in the direction of the magnetic drum where it is collected in a bin, while the magnetic material follows the magnetic drum making it possible to collect it in a separate bin. Using this method, it is possible to divide the bed material in two fractions.

Two samples were collected from the plant at Händelö where a combination of silica sand and ilmenite was used as bed material. The boiler at the Händelö plant was initially operated with silica sand whereas a transition to ilmenite-operation then took place. The bed material was gradually replaced with ilmenite after which the samples were extracted. Two samples were obtained 100 h after the start of the ilmenite feeding. One bottom ash and one fly ash sample, referred to as MSW-FA, were extracted. The bottom ash sample was magnetically separated, and the magnetic fraction was 26%. This sample is referred to as MSW-ilmenite.

The two Örtofta samples were extracted at different occasions. The boiler was operated using ilmenite as bed material for the first 380 h. Thereafter a transition to silica sand operation was initiated and sand was fed back to the boiler. Two bottom ash samples were extracted after 200 h and 580 h from start. Both samples were magnetically separated. The magnetic fraction was 70% for the sample extracted after 200 h of operation and 25% for the sample extracted after 580 h. The sample extracted after 200 h is henceforth referred to as RWW-Ilmenite (3). The sample obtained after 580 h consists of mainly silica sand and was extracted 200 h after the first silica sand input, this sample is referred to as RWW-Sand (4). This sample is used for comparison with MSW-Ilmenite since the bed was mixed with sand. Fresh rock ilmenite, REF, was used as reference for the XPS-analysis.

3.2. Characterization techniques

The total elemental composition of the samples was analyzed using ICP-SMFS according to the standards EN ISO 17294-2: 2016 and EPA-method 200.8: 1994. The soluble chlorine content was determined according to EN ISO 10304–1:2009. These characterizations were performed by the company ALS Scandinavia.

Crystalline bulk phases were determined using powder x-ray diffraction (XRD) with $CuK_{\alpha 1}$ radiation in a Bruker D8 Advanced system. Bottom ash samples were lightly crushed in a mortar before being

analyzed. Scans were made over a 2θ-range between 10º and 90º with a step size of 0.05º and counting time 2s/step. The same settings (40 kV, 40 mA) were used for all samples.

The morphology was examined using scanning electron microscopy (SEM). The microscope is coupled to an energy dispersive x-ray spectroscopy (EDX) which allows study of elemental distribution. Samples were mounted on carbon tape. The system used for this investigation was Quanta 200FEG coupled with an Oxford EDX system. For elemental distribution both point- and elemental map analyses were used.

X-ray photoelectron spectroscopy (XPS) was used for surface material characterization, providing both elemental and chemical state information for solid samples. Another strength with this method is the low detection limits which allows detection of elements down to 0.1 at %. The PHI 5000 VersaProbe III Scanning XPS Microprobe (Base pressure of 1×10^{-9} bar) has been used with monochromated Al-source (25 W) as excitation source. Dual beam flood of low-energy electrons and low-energy argon ions were used to provide charge neutralization during measurements. Spectra was recorded with a 100 μm beam size and pass energy of 224 eV for surveys and 26 eV for high energy resolution measurements. Analysis points were chosen based on x-ray induced secondary electron imaging (SXI) allowing to specify points with good accuracy. Several analyses were performed in each fraction on different particles.

Charge referencing was made to the adventitious C 1s line at 284.8 eV in order to calibrate the binding energies of other elements. The peak areas of each element were normalized by the atomic sensitivity factors (ASF) in the quantitative analyses of the surface composition [45]. Selected region spectra were recorded covering $Pb4f_{7/2}$, $Cu2p_{3/2}$ and $Zn2p_{3/2}$ for the quantification and chemical state identification [45,46]. The high-resolution spectra were fitted using the Multipak software with a Smart background due to the multilevel data. Peak constraints regarding the area ratios and spin-orbit separation were defined as reported in literature [45].

3.3. Thermodynamic study

Thermodynamic calculations were performed using the software FactSage 7.2 [47]. The program consists of calculation and manipulations modules that access different solution databases and substances for calculations of phase diagrams or conditions for multiphase, multicomponent equilibrium. In this study, the module *Equilib* was used. This module requires reactant inputs, temperature, total pressure, possible product phases and solution databases to be specified. The module employs the Gibbs energy minimization principle to calculate the amount of each product at the equilibrium state [47].

Global multicomponent equilibrium calculations were used to study minor and TE interaction with ilmenite during OCAC of waste wood and wood chips and municipal solid waste, representing the conditions at the plant located at Örtofta and Händelö respectively. The thermodynamic databases used for this purpose were FactSage databases FactPS, FToxid and FTsalt. An additional database was included, named HSCA, which contains species originating from HSC Chemistry 9 [48]. The calculations included 59 solid and 79 gaseous species from HSCA. More specifically, this database includes trace elements compounds of As, Co, Cr, Cu, Mn, Mo, Ni, Pb, V and Zn. Hence, it is believed that the quality of the calculations is improved with respect to these species.

The global calculations were performed at 850 °C and atmospheric pressure. The fuels are of heterogeneous nature and there was no analysis done with respect to composition of the fuel for the two boilers. Hence, the elemental composition of the RWW fuel mixture consisting of 50% recovered waste wood with the rest being equal amounts of wood chips and treetops/branches was estimated from the mean compositions of each fuel fraction as reported by Strömberg, B [21]. The MSW-composition was estimated using the average of six different MSW elemental analyses as reported by Avfall Sverige [49]. As it is clear that the MSW fuel composition can vary, thermodynamic calculations were

Table 1
Summary of samples analyzed in this paper.

Sample	Acronym	Origin	Load (MW$_{th}$)	Type	Fuel (50:50)
1	MSW-Ilmenite	Händelö	75	Bottom Ash	Municipal solid waste and industrial solid waste
2	MSW-FA	Händelö	75	Fly Ash	Municipal solid waste and industrial solid waste
3	RWW-Ilmenite	Örtofta	115	Bottom Ash	Recovered waste wood and wood chips
4	RWW-Sand	Örtofta	115	Bottom Ash	Recovered waste wood and wood chips
5	REF	Fresh sample	–	–	–

performed using the six reported fuel compositions and compared with the calculated mean value. The difference in phase formation and trace element speciation was studied. No major difference with respect to trace element speciation were found, and hence it is believed that the average value gives a reasonable description of the fuel and its components. The fuel contents are presented in normalized weight percent in Table 2.

Fig. 2 illustrates the methodology for the two different thermodynamic calculations performed in this study. The global equilibrium calculations are performed using the fuel composition, Table 2, air and an excess amount of the bed material ilmenite ($FeTiO_3$) as input. The amount of ilmenite was defined as five times the weight input of the fuel. This resulted in the bed consisting of roughly 95% ilmenite and 5% ash. The excess is defined to maintain an ilmenite rich bed. The air flow was varied in order to study the effect of different reduction potentials, since the oxygen partial pressure may vary locally in the boiler and inside the particles. The reduction potential is expressed as the logarithmic ratio pCO/pCO_2. Higher reduction potentials represent conditions further into the particle, closer to the fuel particles and oxygen deficient parts of a boiler. Additionally, higher reduction potentials may provide an insight for possible compound formation in a CLC fuel reactor. The output from the calculations provides equilibrium compositions of the gas, solids and solid solutions.

These calculations result in useful information about the general behaviour of the trace elements. The final global calculation consisted of 103 solutions and 1959 species distributed as 730 solution phases, 524 gas compounds and 705 pure solids. Local thermodynamic calculations, illustrated in Fig. 2, were performed with the same databases and settings. The calculation is performed locally on one particle and the input is based on the surface composition obtained from the XPS-analysis. These calculations were then performed in a similar way as above but using 71 solution phases and 1299 species distributed as 529 solution species, 220 gas compounds and 550 pure solids.

4. Results

The elemental composition of the samples is presented in Table 3.

Table 2
Fuel composition of the two calculated fuel mixtures MSW and RWW.

| Species	Unit	RWW	MSW
Ash content	wt%	3.7	13.05
Moisture	wt%	26.4	37.1
C	wt% daf	36.2	29.1
H	wt% daf	4.4	3.8
O	wt% daf	28.7	15.4
S	wt% daf	0.04	0.38
N	wt% daf	0.55	0.70
Cl	wt% daf	0.02	0.50
Al	wt%	0.21	1.5
Ca	wt%	1.3	3.6
Fe	wt%	0.15	0.81
K	wt%	0.5	0.39
Mg	wt%	0.17	0.44
Mn	wt%	0.09	0.02
Na	wt%	0.10	0.81
Si	wt%	1.0	4.8
Ti	wt%	0.08	0.24
P	wt%	0.08	0.10
As	mg/kg	20	29
Ba	mg/kg	267	335
Cd	mg/kg	0.39	4.14
Co	mg/kg	1.2	9.5
Cr	mg/kg	48	219
Cu	mg/kg	32	876
Mo	mg/kg	0.7	10.8
Ni	mg/kg	3.9	200
Pb	mg/kg	28	760
V	mg/kg	2.0	15
Zn	mg/kg	583	969
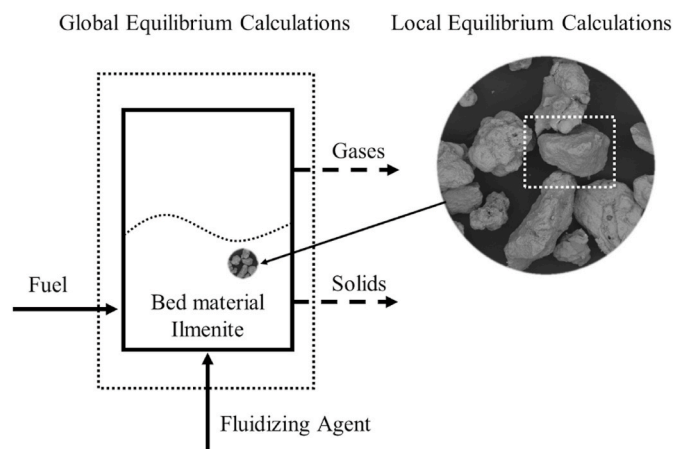
Fig. 2. Description of the fluidized bed boiler and clarification of global and local thermodynamic calculations. Solid arrows represent the input and dashed arrows represent the output.

Table 3
Elemental composition of selected magnetically separated samples as provided by ALS Scandinavia. The reference is reported as received from supplier.

Sample [mg/kg]	REF*	MSW-Ilmenite (1)	MSW-FA (2)	RWW-Ilmenite (3)	RWW-Sand (4)
Si	9400	95 500	86 300	47 500	257 000
Ca	2600	90 300	194 000	108 000	81 700
Fe	332 900	162 000	24 200	190 000	21 300
Ti	238 500	93 400	12 500	160 000	15 500
Al	3400	24 900	77 700	15 000	30 300
Mg	18 300	16 100	15 500	20 200	10 700
Na	800	12 100	21 900	9600	12 900
K	700	4650	12 200	18 200	43 100
Mn	1300	2110	1070	5720	4580
S	–	8990	27200	7230	1720
Cl	–	500	72000	26	17
Zn	100	8650	7400	10 100	10 400
Cu	100	3180	5040	810	702
Pb	<0.0001	686	2280	675	544
Cr	–	677	444	883	203

The table shows that the bed sample MSW-Ilmenite (1) contain slightly higher amounts of Si and Al and slightly lower amount of Fe and Ti compared to RWW-Ilmenite (3). However, the Si contents are far from the one in RWW-Sand (4) which has a different composition with respect to all major elements. The main elements in the fly ash MSW-FA (2) are Ca, Si, Al and Cl and S.

The Zn-content is similar in all fractions with slightly lower amounts in the fly ash MSW-FA (2). Pb content is similar in all bottom ash fractions with higher amount in the fly ash MSW-FA (2). Higher amounts of Cu are detected in both samples from Händelö, likely due to the fuel.

4.1. Global thermodynamic equilibrium calculations

The phase composition of ilmenite will depend on the reduction potential in the boiler as different regions may be air-rich or air-lean. The oxygen carrying capability of ilmenite depends on the transition between Fe^{2+} and Fe^{3+}. The most reduced form is $FeTiO_3$ ($FeO + TiO_2$) and the most oxidized form is Fe_2TiO_5 ($Fe_2O_3 + TiO_2$) [50]. Thus, the results from the thermodynamic calculations are divided into three different regions depending on the phase formation. Oxidizing conditions are defined where Fe_2TiO_5 ($Fe_2O_3+TiO_2$) is the stable phase. This occurs between the reduction potentials $\log_{10}[pCO/pCO_2] = -8.0$ and -4.5. Spinel (Fe_3O_4) formation starts and ends around the reduction potentials -5.0 and -3.0 respectively, corresponding to oxygen partial pressures between $\log_{10}[pO_2] = -7.2$ and -11.2 atm. These are defined

as moderately reducing conditions and could represent conditions relevant in oxygen deficient areas in OCAC. The highly reducing conditions occur above the reduction potential -2.0 where ilmenite ($FeTiO_3$) starts to form. Higher reduction potentials represent conditions further into the particle or closer to the fuel particles. At even higher reduction potentials, around $\log_{10}[pCO/pCO_2] = 1.6$ and $\log_{10}[pO_2] = -20.4$ atm graphite is expected to form. Table 4 illustrates the different defined regions along with their corresponding reduction potential, oxygen partial pressure and the CO_2-yield.

Fig. 3 illustrates the solid phase distribution across different reduction potentials for the calculation with MSW. The corresponding figure for RWW is presented in Fig. S1 in supplementary material. On the secondary y-axis the logarithmic oxygen partial pressure is presented over a range from approximately 0.06 atm to $3.2 \cdot 10^{-18}$ atm. Further decrease of the oxygen content would result in formation of metallic species which are likely not relevant for the materials studied in this paper. Fig. 3 clearly shows that the bed consists of a large fraction ilmenite, allowing trace element interactions with ilmenite particles to be studied.

In the highly reducing environment the phases ilmenite ($FeTiO_3$), titania spinel ($FeTi_2O_4$) and wollastonite ($CaSiO_3$) are formed, with a small amount of slag. During moderately reducing conditions the main phases are rutile (TiO_2) and spinel (Fe_3O_4) while corundum (Fe_2O_3) and rutile (TiO_2) are formed in the oxidizing environments, below the reduction potential -4.5. Smaller amounts of feldspar ($(K,Na)AlSi_3O_8$) and perovskite ($CaTiO_3$) are formed across the whole range. The amount of slag was slightly higher in the case with RWW and was formed across the whole range of investigated gas compositions.

4.1.1. Fate of trace elements for municipal solid waste

Results for the case at the Händelö plant using MSW as fuel are compiled in the figures below. Fate of trace elements were evaluated at different reduction potentials illustrated in Figs. 4–6 showing the phase distributions of zinc, copper and lead.

Fig. 4 shows that zinc forms a spinel compound across the whole range. In the oxidizing environment $ZnFe_2O_4$ is stable, but when increasing the reduction potential above -1.9 $ZnCr_2O_4$ becomes the stable phase. At the reduction potential -1.9 a large fraction (53%) of willemite ($Zn,Fe)_2SiO_4$ is formed. When going from moderately reducing to highly reducing conditions the main spinel phase (Fe_3O_4) will decrease and the ilmenite phase ($FeTiO_3$) will increase, as seen in Fig. 3. This transformation will likely hinder zinc from entering the spinel phase. Therefore, Zn will start to interact with silica forming willemite. When increasing the reduction potential above -1.9 (corresponding to a $\log_{10}[pO_2]$ of -13.5 atm) zinc will start to enter the gas phase, mainly as Zn (g). At the reduction potential -1.1 ($\log_{10}[pO_2] = -15.1$ atm) around 61% of the zinc is retained as solids (45% in the slag phase as ZnS and 14% as spinel, mainly $ZnCr_2O_4$). Further reduction pushes the equilibrium of Zn towards the gas phase, Zn (g). Thus, for the more reducing conditions, as more zinc is released to the gas phase, it is

more prone to end up in the fly ash.

The copper phase distribution is presented in Fig. 5. It shows that from oxidizing to moderately reducing conditions a gas phase is formed which mainly consists of $(CuCl)_3$ (g). Under oxidizing conditions copper preferably interacts with iron to form $CuFe_2O_4$ (s) and with increasing reduction potential $Cu_2Fe_2O_4$ (s) and then Cu (s). When reaching highly reducing conditions, above the reduction potential -1.9, a slag phase with Cu_2S is formed accompanied by some Cu_3As (s) under highly reducing conditions.

The lead phase distribution is presented in Fig. 6. Pb is distributed mainly in gaseous compounds which range from $PbCl_2$ (g) in the oxidizing and moderately reducing environment parts, to PbS (g) which is the main constituent in the highly reducing environment. At the reduction potential 0.1 PbS (g) is accompanied by Pb (g). A small fraction of lead (approximately 5%) is dissolved in a slag phase containing PbS under highly reducing conditions.

4.1.2. Fate of trace elements for recovered waste wood

Results for the case at the Örtofta plant utilizing the fuel mixture recovered waste wood and wood chips are compiled and presented in the supplementary material. For the case with RWW, presented in Fig. S2, most of the zinc will form spinel in combination with iron, $ZnFe_2O_4$, similar to what was seen for MSW in Fig. 4. When highly reducing conditions are employed, above the reduction potential -1.9, formation of $ZnCr_2O_4$ is preferred. At the reduction potential -1.9, willemite, $(Zn,Fe)_2SiO_4$, forms together with Zn (g) and a small amount of ZnO dissolves into a slag phase. Further reduction pushes the equilibrium towards the gas phase which mainly consists of Zn(g). As opposed to the gas composition in Fig. 4, over 85% zinc enters gas phase as Zn (g) when reaching the reduction potential -1.1. The gaseous compounds $ZnCl_2$, $KZnCl_3$ and $Zn(OH)_2$ are formed at oxidizing and moderately reducing conditions but the amount of gas formed at these conditions is negligible.

The copper content is significantly lower in the recovered waste wood and wood chips compared to MSW, Table 2. For oxidizing and moderately reducing conditions the major constituent is Cu_2O dissolved in a slag phase, presented in Fig. S3. The amount of gas never exceeds 0.6% showing that copper is retained in the bottom ash under all conditions. When entering highly reducing conditions, exceeding the reduction potential -1.9, the solid compounds Cu_3As (s) becomes the major phase (above 88%). RWW contains relatively high arsenic content, approximately one third of the copper concentration, which favors the formation of Cu_3As (s). If the As-content is lowered, the amount of gas is expected to increase at high reducing potentials, forming a larger amount copper chloride accompanied with smaller amounts of copper in the slag phase. As likely originates from wood preservatives such as chromated copper arsenate (CCA). EU has introduced restrictions against CCA since 2004, which has lowered the amount of CCA-treated wood since [51]. However, arsenic may still enter the waste streams since substantial quantities of CCA have been used daily and for a long

Table 4
The relation between the logarithmic reduction potential, logarithmic oxygen partial pressure and the yield of CO_2.

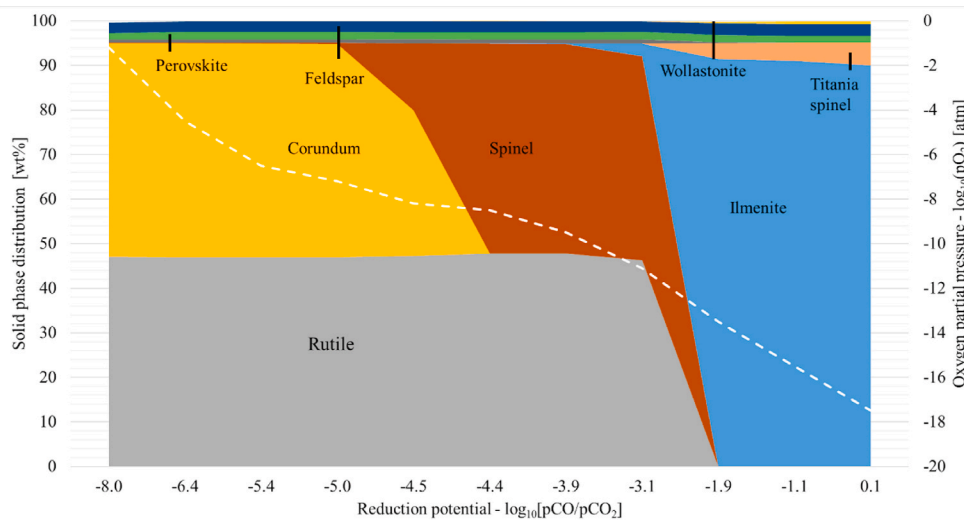| Logarithmic reduction potential	Corresponding oxygen partial pressure		CO_2 yield
$\log_{10}[pCO/pCO_2]$	$\log_{10}[pO_2]$	Condition	$\dfrac{pCO_2}{pCO + pCO_2}$
-8.0	-1.2		
-5.4	-6.5	Oxidizing	> 0.9999
-5.0	-7.2		
-4.5	-8.2	Moderately reducing	$0.9999 > \dfrac{pCO_2}{pCO + pCO_2} > 0.9990$
-3.0	-11.2		
-1.9	-13.5		0.986
-1.1	-15.1	Highly reducing	0.920
0.1	-17.5		0.420

Fig. 3. Solid phase distribution of the main solids formed for MSW using ilmenite as bed material. Calculations were performed at 850 °C and a range of different reduction potentials. The main constituents of the phases in the diagram are ilmenite ($FeTiO_3$), titania spinel ($FeTi_2O_4$), wollastonite ($CaSiO_3$), rutile (TiO_2), spinel (Fe_3O_4), corundum (Fe_2O_3), feldspar ((K,Na)$AlSi_3O_8$) and perovskite ($CaTiO_3$). The white dashed line represents the corresponding logarithmic oxygen partial pressure.
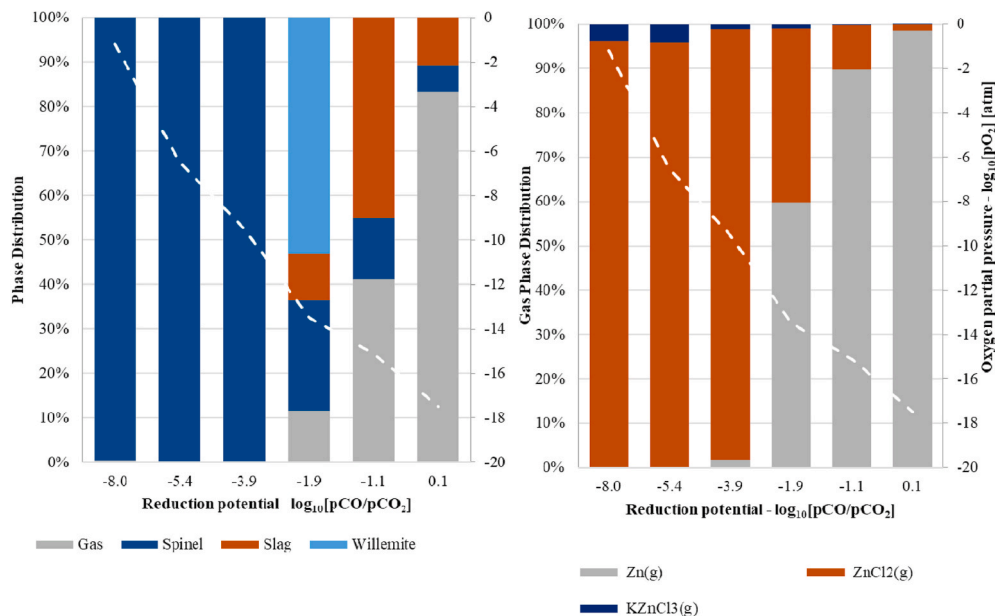

Fig. 4. Zinc phase distribution under OCAC conditions using ilmenite as bed material and municipal solid waste as fuel. Calculations are performed at atmospheric pressure and 850 °C. The white dashed line represents the corresponding logarithmic oxygen partial pressure presented on the secondary y-axis.

time but could also be due to imported waste wood. There are currently no EU directives stating that CCA-treated wood should be removed from their current applications. Therefore, it is expected to remain in use for some years to come. Thus, CCA treated wood can be expected to be found in waste fuels and affect the speciation of Cu species.

The MSW composition presented in Table 2 contains higher amounts of Cl and S compared to RWW, which has important implications on the results. This is reflected in the thermodynamic results where the gas phases of zinc, copper and lead in the case with MSW contain larger fraction of chlorides in comparison to RWW. It is known from literature that Cl may enhance the volatility of several heavy metals while S may decrease volatility due to formation of condensed sulphate phases [30, 52]. When comparing the lead phase distribution between the fuels significantly less chlorides are formed for RWW, and significantly larger fraction is kept in the slag phase in oxidizing and at moderately reducing conditions, see Fig. S4. This is likely due to the higher fraction of K compared to Cl in RWW. This allows more K to be associated with Si, favoring slag phase formation. Pb is then selectively dissolved in this

phase, and the small Cl content will hinder formation of lead chlorides in the gas phase. The slag phase, which is formed with RWW consists of oxides (ZnO, PbO and Cu_2O) while the slag phase formed for MSW dominates in moderately and highly reducing conditions and contains sulfide compounds (ZnS, PbS and Cu_2S).

An additional database, HSCA, was used in this study which includes more compounds not present in the standard FactSage databases. The database allowed additional gaseous and solid compounds to form, improving the calculations. The effects are noticed in the MSW calculations as several predicted gaseous compounds originate from HSCA. For example the gas phase distributions of Cu and Pb in Figs. 5 and 6, where $CuCl_2$ (g), Cu_2Cl_2 (g) and Pb_2O_3 (g) form. For the RWW calculation the effect is noticed in the zinc and copper distribution where Zn $(OH)_2$ (g) and CuH (g) form. Thus, the database is important in order to describe these systems accurately.

Fig. 5. Copper phase distribution under OCAC conditions using ilmenite as bed material and municipal solid waste as fuel. Calculations are performed at atmospheric pressure and 850 °C. The white dashed line represents the corresponding logarithmic oxygen partial pressure presented on the secondary y-axis.
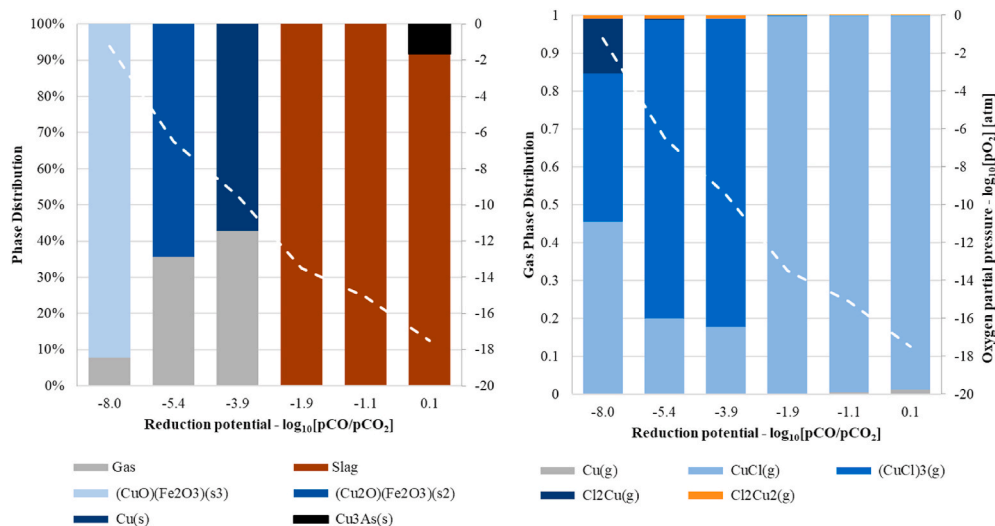

Fig. 6. Lead phase distribution under OCAC conditions using ilmenite as bed material and municipal solid waste as fuel. Calculations are performed at atmospheric pressure and 850 °C. The white dashed line represents the corresponding logarithmic oxygen partial pressure presented on the secondary y-axis.
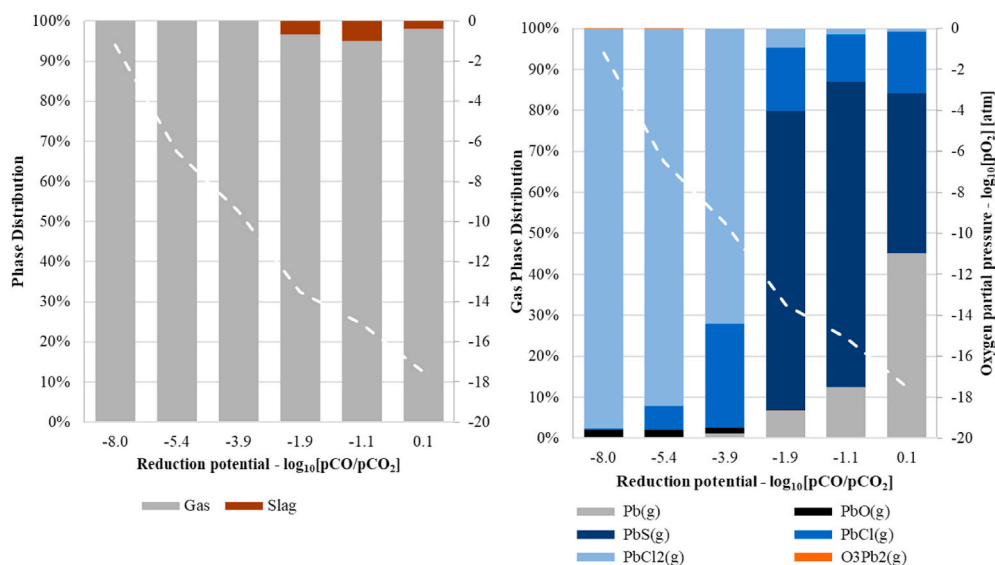
4.2. Phase composition and surface morphology

The main crystalline phases as determined by XRD for both MSW-Ilmenite (1) and RWW-Ilmenite (3) are aligned with the results obtained from the thermodynamic calculations (Fig. 3). The phases detected in the two ilmenite bottom ash samples MSW-Ilmenite (1) and RWW-Ilmenite (1) were iron titanium oxide $Fe_3Ti_3O_{10}$ ($Fe_3O_4 + 3\ TiO_2$), rutile (TiO_2), perovskite ($CaFe_xTi_{1-x}O_3$), spinel ($Mg_{1-x}Zn_xFe_2O_4$), quartz (SiO_2), feldspar ((K,Na)$AlSi_3O_8$), melilite ((Ca_xNa_{2-x})($Mg_yFe_zAl_{1-y-z}$)Si_2O_7) and traces of other silicates ($K(Zn_x,Mn_{3-x},Fe_y,Mn_{2-y})Si_{12}O_{30}$)). With respect to the observed bulk phases and their oxidation state, it is important to consider that the particles have likely been exposed to conditions between oxidizing and moderately reducing environments. Fig. 3 shows that the spinel and rutile phases are stable here. The particle surface on the other hand is in contact with the gas phase where the average oxygen partial pressure ranges between 0.21 and 0.04, i.e. oxidizing environment. However, the particles may be exposed to more reducing environments locally.

Phases with the elements copper and lead were difficult to observe

with XRD due to the low content. However, some impurities could be observed, such as $Mg_{0.4}Zn_{0.6}Fe_2O_4$ for both MSW-Ilmenite (1) and RWW-Ilmenite (3). Traces of zinc silicates could also be observed, which could be a possible interaction path when using silica sand as bed material. Thus, it is likely that locations with higher silica sand concentrations in the bed could result in zinc incorporating in silicates. This was also predicted in the thermodynamic calculations where willemite was formed at moderately reducing conditions.

Surface features of the three industrial samples are illustrated in Fig. 7, as determined by scanning electron microscopy. Chemical mapping was performed on a large area to observe trends in composition. The elemental mapping, see Fig. S5 in supplementary material, indicated the presence of lead in submicron particles in MSW-FA (2) while larger particles, pieces of the bed material, could contain a major amount of potassium, aluminum and silicon or iron and calcium. Zinc and copper were also detected, unevenly distributed across the sample. XRD confirmed the formation of calcium sulfate, melilite and elemental aluminum in MSW-FA (2).

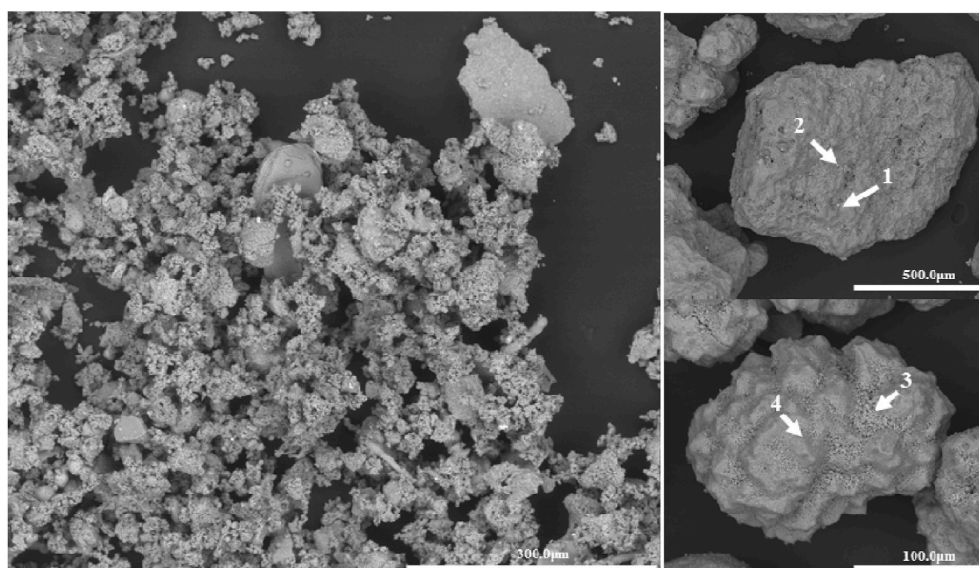Mappings were performed on a larger area to observe trends in

Fig. 7. Electron micrographs of the particle surfaces, taken with SSD-detector. Sample MSW-FA (2) to the left, MSW-Ilmenite (1) upper right and RWW-Ilmenite (3) lower right. Position for point analyses are indicated in the figures.

Table 5
Elemental composition (at %) of selected points of the SEM-EDX analysis in Fig. 7.

Sample	MSW-Ilmenite (1)	MSW-Ilmenite (1)	RWW-Ilmenite (3)	RWW-Ilmenite (3)
Position	1	2	3	4
Mg	–	4.6	6	3.7
Al	1.6	8.8	–	–
Si	4.1	13.9	1.2	1
Ca	5.9	10.2	3.4	2.8
Ti	–	1.5	7.9	6.2
Fe	28.4	7.4	15.6	6.7
Cu	2.2	–	–	–
Zn	12.4	1.1	1.5	0.4

composition. Thereafter several point analyses were performed and two of these, from each bottom ash fraction, are presented in Table 5. Mapping of the particles from MSW-Ilmenite (1) found that zinc covers the surface of the ilmenite bottom ash samples, either in combination with Al, Fe or Mg. See Figs. S6–8 in supplementary material. Copper could also be observed in some cases with higher intensity in distinctive points. Point analyses were performed on the surfaces for MSW-Ilmenite (1) and RWW-Ilmenite (3), pointed out in Fig. 7, to confirm the presence of Zn and Cu. Position 1 was chosen based on the higher Zn-content from the mapping analysis, and positions 2–4 to investigate the average amount of Zn. Table 5 shows the main ash forming elements together with the elements Cu and Zn, with positions indicated in Fig. 7.

The results in Table 5 are well aligned with the findings from the global equilibrium calculations where zinc is found in a spinel formation as seen in Fig. 4. In position 1, showed in Fig. 7, the Zn:Fe ratio is ~1:2 suggesting a spinel structure. The lower amount of copper makes detection with SEM-EDX difficult. Point analyses show that the average Zn-content is around 1 at% on the surfaces of particles in both bottom ash fractions. The content of Pb was below the detection limit and therefore it was not possible to draw a conclusion using this approach.

4.3. Chemical speciation of particle surfaces

X-ray Photoelectron Spectroscopy (XPS) was performed to evaluate the outermost layer of the particles in detail. This layer is in contact with the gas phase and can be one interaction channel for ash components in both the boiler and downstream of the main combustion chamber.

Fig. 8 shows the XPS spectra for the four samples as well as the reference material. The XPS-analyses performed use a beam size of 100 μm which provide information about the surface of the bottom ash particles but a mean composition of several submicron particles for the fly ash sample. Several survey analyses were performed in each fraction, but one is shown here for comparison. The survey spectrum shows the photoelectron peaks which are characteristic for each element at the surface of each particle. Comparison with the fresh sample REF (5) shows accumulation of elements in both bed samples, i.e. MSW-Ilmenite (1) and RWW-Ilmenite (3). The Fe, Ti and Mg peaks have slightly lower intensities while Na, Ca, K and S increase accompanied by minor elements such as P, Zn, Cu and Pb. RWW-Ilmenite (3) showed slightly higher content of Fe and Ti at the surface compared to MSW-Ilmenite (1) which instead contained higher amounts of Ca, Al and Si. The survey for MSW-FA (2) shows that the submicron particles are enriched in Ca, K, Cl accompanied by minor amounts of Zn, Al, S, Cu and F.

The XPS survey quantification, presented in Table 6, allows detection of elements on the surfaces of the bed material which is not possible using other characterization techniques such as SEM-EDX. Several point analyses performed showed that Zn and Cu were detected to be slightly above 0.5 at%. Pb was also detected in all samples except MSW-Ilmenite (1) where the concentration was <0.1%.

In order to obtain more detailed information regarding the chemical states of zinc, copper and lead, high-resolution analysis was performed. The high-resolution analysis is performed with lower pass energy and narrow region, which is unique for each element. The spectral regions Cu 2p, Zn 2p and Pb 4f were selected for this purpose as no overlapping is detected for these species, and as they are also the focus of this specific work.

4.3.1. Chemical state investigation - copper

The spectral region for Cu 2p is located at binding energies between 930 eV and 960 eV. The XPS-quantification procedure for Cu-species incorporate the use of shake-up lines and binding energies of the main peak. It is known that Cu^{2+} may be identified using the strong shake-up satellite adjacent to the main Cu $2p_{3/2}$ peak [53]. This peak is almost not present in the case of metal Cu but may be present as a weak peak for Cu^+ compounds. Additionally, the corresponding Cu LMM line can be useful for further chemical state analysis. However, in this study the Auger peak was difficult to obtain because of the overlapping Ti 2s peak
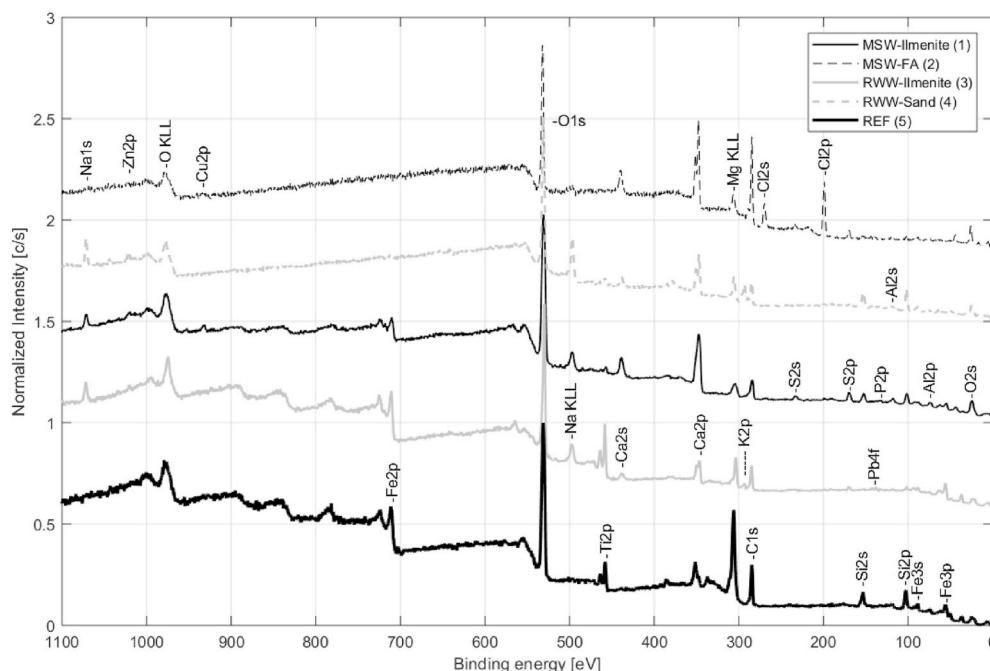
Fig. 8. Survey spectrum recorded with pass energy 224 eV for ilmenite particles obtained from MSW-Ilmenite (1) RWW-Ilmenite (3), RWW-Sand (4), REF (5) and the fly ash MSW-FA (2).

Table 6
Elemental composition in atomic percent obtained from the XPS quantification using standardized atomic sensitivity factors (ASF).

Sample [at%]	Peak	MSW-Ilmenite (1)	MSW-FA (2)	RWW-Ilmenite (3)	RWW-Sand (4)
O	**1s**	65.4	56.1	62.6	62.7
Ca	**2p**	10.3	14.6	4.9	6.7
Si	**2p**	6.3	2.4	2.4	12.3
Al	**2s**	4.8	3.7	2.1	0.9
Fe	**2p**	4.1	2.0	10.0	1.5
S	**2p**	3.3	2.7	1.3	0.5
Na	**1s**	2.8	0.0	3.9	6.1
P	**2p**	0.8	0.0	0.7	1.2
Cu	**2p3/2**	0.7	1.7	0.0	0.0
Ti	**2p**	0.6	0.0	7.5	1.3
Zn	**2p3/2**	0.6	0.7	0.6	0.8
Cl	**2p**	0.2	14.8	0.5	0.6
Mg	**2p**	0.1	0.7	2.8	1.6
Pb	**4f**	0.0	0.2	0.1	0.1
Mn	**2p**	0.0	0.0	0.0	1.0
K	**2p**	0.0	0.3	0.6	2.8

or low intensity. Copper compounds have been thoroughly studied in literature [53]. $CuFe_2O_4$ has binding energies close to those of CuO and similar satellite structures [54]. The peak position reported in literature for CuO is 933.1 eV, while $CuFe_2O_4$ has been reported to have a binding energy of 933.2 eV [55]. However, the satellite for $CuFe_2O_4$ is reported to occur at 942.8 eV with lower intensities compared to CuO [55].

Fig. 9 shows the high-resolution scans for each sample and specie together with the fitted components. Copper was observed in the samples MSW-Ilmenite (1) and MSW-FA (2). The two RWW samples did not indicate any copper content at the surface, most likely due to the low content in the fuel mixture. The intensity of the observed Cu 2p peaks were high and the peaks were narrow. The peaks were fitted using the spin orbit splitting together with the positions 933.2 eV, 952.8 eV and 942.8 eV, corresponding to the Cu $2p_{3/2}$, Cu $2p_{1/2}$ and satellite peak as reported in literature for $CuFe_2O_4$ [55]. The same full width half maximum was used for all chemical states (FWHM = 2 eV). An additional peak located at 935.2 eV was used for the fly ash, corresponding to $CuCl_2$ [56]. Results show that approximately 80% of Cu is bonded as an oxide with the rest being copper chlorides in the fly ash. The fitted components presented in Fig. 9 are well aligned with the experimental data from the literature, confirming the formation of $CuFe_2O_4$ and $CuCl_2$.
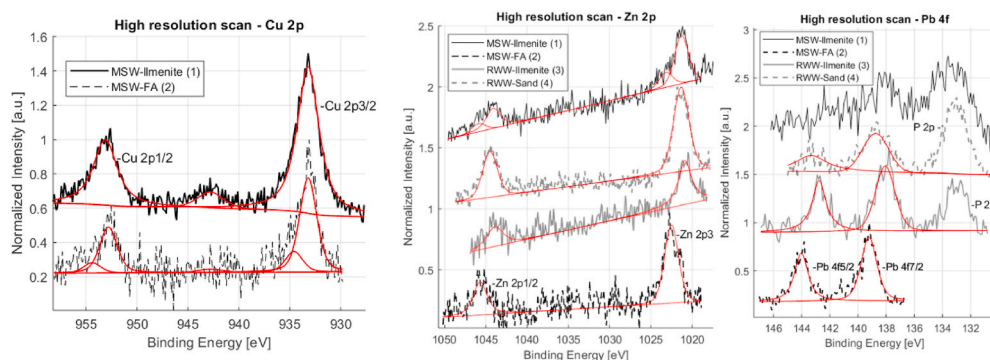

Fig. 9. High resolution scans of Cu 2p (left), Zn 2p (middle) and Pb 4f (right). Spin orbit splitting indicated in the figure together with the fitted components.

4.3.2. Chemical state investigation - zinc

The spectral region for Zn 2p is located at binding energies between 1019 eV and 1050 eV. The high-resolution spectra for Zn 2p are presented in Fig. 9. The chemical state analysis may be performed using the binding energies and corresponding Zn LMM peak. However, in this study the intensity of the Zn LMM Auger peak was too low for all samples in order to confirm the chemical state. Thus, chemical states are compared with experimental data reported in literature using the same experimental settings [57]. The binding energy for the main peak Zn $2p_{3/2}$ of $ZnFe_2O_4$ has been reported to be 1021.6 eV [58]. It is known that the photoelectron peak of Zn $2p_{3/2}$ in tetrahedral and octahedral sites of ferrites can be observed with an energy difference around 1.9 eV. Zinc atoms occupying tetrahedral sites may be ascribed to the binding energy 1021.3 eV while peaks with the binding energy 1023.2 eV correspond to incorporation of Zn^{2+} ions at octahedral sites [59]. The interaction between zinc ions and alumina has been studied by Strohmeier et al. [60] The study showed that low zinc loadings allows formation of a spinel phase where zinc ions occupy tetrahedral sites. One study, using similar settings as this paper, reported $ZnO/ZnAl_2O_4$ composites to have the binding energies 1022.4 eV and 1045.7 eV for Zn $2p_{3/2}$ and Zn $2p_{1/2}$ respectively [61].

The MSW-Ilmenite (1) spectra was fitted using two parameters due to the broad peak. The peak positions 1021.3 eV and 1023.2 eV were used in the fitting process corresponding to Zn^{2+} ions occupying either tetrahedral or octahedral sites. It is observed that 83% belongs to Zn^{2+} ions occupying tetrahedral sites. The peak for MSW-FA (2) was 1022.5 eV, close to the reported value of $ZnAl_2O_4$. The peak position for Zn $2p_{3/2}$ in RWW-Sand (4) is found to be 1021.3 eV. The XPS-quantification results for sample RWW-Sand (4), Table 6, shows that the ratio between Zn:Fe is ~1:2 indicating that there is enough iron to form $ZnFe_2O_4$. The corresponding peak for RWW-Ilmenite (3) is positioned at 1021.3 eV, aligned with the reported value of $ZnFe_2O_4$.

4.3.3. Chemical state investigation - lead

The spectral region for Pb 4f is located at binding energies between 136 eV and 146 eV. The high-resolution spectra for Pb 4f are presented in Fig. 9. Previous studies have been made investigating various lead compounds using XPS [62]. The peak position for MSW-FA (2) is 139.2 eV which is in the range of $PbCl_2$ as reported in literature [62]. The position for RWW-Ilmenite (3) is found to be 137.9 eV corresponding to $PbTiO_3$ while RWW-Sand (4) has a position at 138.8 eV related to $PbSiO_3$ [62]. The sample MSW-Ilmenite (1) indicates that lead could be present, Fig. 9, but due to the low concentration the peaks were not fitted. However, the peaks are visually like those of RWW-Ilmenite (3). This could indicate that lead is buried beneath the top surface. A summary of the phases detected in each sample is presented in Table 7.

4.3.4. Comparison with local thermodynamic equilibrium calculations

Local thermodynamic equilibrium calculations are performed based on the quantification results from the survey analysis presented in Table 6. The final calculations consisted of 71 solution phases and 1299 species distributed as 529 solution species, 220 gas compounds and 550 pure solids. The temperature was set to 850 °C for the bottom ashes and 250 °C for the fly ash calculation. Results from the local thermodynamic calculations are presented in Table 8. The surrounding gas phase was set to consist of 5% O_2, which is a mean value for the concentration of

oxygen in the gas outlet from the boilers.

The local thermodynamic calculations predict spinel-compounds in each fraction with some amounts of olivine in RWW-Sand (4). The chemical states are in accordance with the local thermodynamic calculations which predicted ferrites and lead oxides in the bottom ash and zinc aluminate and condensed lead chlorides in the fly ash. However, some discrepancies are also observed. The formation of PbO in RWW-Sand and $(CuO)(Fe_2O_3)$ in MSW-FA are two compounds not completely aligned with the experimental findings. Formation of $(CuO)(Fe_2O_3)$ is stable across temperature regions between 100 °C and 900 °C and could end up in the fly ash together with entrained bed particles. Several analyses showed that the concentration of copper was slightly higher in larger particles (>50 μm). Submicron particles are inevitably characterized along with these larger particles in the fly ash, which could affect the thermodynamic outcome as the mixing is not optimal.

Studying the $PbO–SiO_2$ phase diagram shows that lower amounts of Pb favors slag phase formation above 750 °C while lead silicates are favored below 750 °C explaining why thermodynamic calculations predict a slag phase. The $PbO–TiO_2$ phase diagram on the other hand shows that $(PbO)(TiO_2)$ is stable across the whole region with one small region forming a slag phase at high contents of Pb (>99.5%). Other explanations could be due to not reaching equilibrium or kinetic limitations since the calculations assume perfect mixing and infinite reaction time. Nonetheless, these thermodynamic calculations have shown to be useful and consistent with the experimental findings. Thus, including silica sand during biomass combustion could provide some additional possibilities to retain lead in the bottom ash.

5. Discussion

This study presents an investigation of the interaction between ilmenite and two different waste fuels at two commercial CFB units employing oxygen carrier aided combustion, or OCAC. The focus has been on the fate of trace elements, where both detailed characterization techniques and thermodynamic equilibrium approaches have been used for increased understanding. The trace elements Pb, Zn and Cu have been in focus, which are species that can be found at significant levels in various waste fuels. The use of oxygen carriers in normal fluidized bed combustion could have advantages with respect to combustion efficiency and gaseous emissions. Further, there could be potential benefits with respect to the fate of reactive ash components, as these could react with the oxygen carrier to form stable compounds. In normal combustion, these species are known to react with chlorine to highly volatile species, which could evaporate and be precursors for corrosion phenomena downstream of the main boiler. Hence it is important to study the fate of these elements using oxygen carriers. This study focuses on ilmenite, which is a benchmark oxygen carrier, and as it contains Fe, the results should be highly applicable for other types of Fe-based oxygen carriers [63].

The results here are applicable on OCAC-systems as discussed throughout this paper. However, the results can be highly relevant for other systems using oxygen carriers, for example chemical-looping combustion (CLC) and chemical looping gasification (CLG) [64]. The global thermodynamic calculations were performed at various reducing potentials, which are relevant for these three technologies. Further, it can be expected that the particles in a CFB boiler could be exposed to variable oxidizing and reducing conditions even in the same reactor [65]. Hence, it can be presumed that many of the reaction pathways of the oxygen carriers and ash components could be the same. Of course, the residence times at different reducing potentials and actual contact with ash components could be different. In a CLC and CLG system it is not expected that any fuel conversion would take place in the air reactor, and hence any transformations in this reactor would likely stem from transfer of particles from the fuel reactor, both oxygen carriers and ash.

The degree to which the oxygen carrier reacts with the trace elements is highly dependent upon the degree of reduction in the reactor. In

Table 7
Summary of phases identified using XPS.

Sample Specie	MSW-Ilmenite (1)	MSW-FA (2)	RWW-Ilmenite (3)	RWW-Sand (4)
Copper	$(CuO)(Fe_2O_3)$	$(CuO)(Fe_2O_3)$ $CuCl_2$	–	–
Zinc	$ZnFe_2O_4$	$ZnAl_2O_4$	$ZnFe_2O_4$	$ZnFe_2O_4$
Lead	–	$PbCl_2$	$(PbO)(TiO_2)$	$(PbO)(SiO_2)$

Table 8

Main phases formed for zinc, copper and lead based on local thermodynamic calculations.

| Sample | MSW-Ilmenite (1) | | MSW-FA (2) [a] | | RWW-Ilmenite (3) | | RWW-Sand (4) | |
Specie								
Copper	$(CuO)(Fe_2O_3)$	(s)	CuO	(s)	–	–	–	–
Zinc	$ZnFe_2O_4$	Spinel	$ZnAl_2O_4$	Spinel	$ZnFe_2O_4$	Spinel	$ZnFe_2O_4$	Spinel
					$ZnMg_2O_4$	Spinel	$MZnSiO_4$	OlivA
Lead	–	–	$PbCl_2$	(s)	$(PbO)(TiO_2)$	(s)	PbO	SlagA

M for Mg, Zn, Ca (according to amount).

[a] Calculations performed at 250 °C.

the calculations and in the detailed characterization all three species can react to combined oxides such as copper ferrites, zinc ferrites and lead titanium oxides under oxidizing conditions, see Figs. 4–6 and Table 7. These mixed oxides could be stable in the oxygen carrier particles and they could also have oxygen carrying capabilities. For example, copper ferrites [66–68] and zinc ferrites [69] have previously been studied as oxygen carriers. This opens for the possibility to increase oxygen carrying capacity of the bed as the residence time increases, something which would be highly beneficial.

From the global equilibrium calculations, it is clear that there are some differences in the fate of the trace elements depending upon the gas phase. For example, Zn is more prone to enter the gas phase, as the degree of reduction potential increases, something which could be highly relevant if Zn is to be recovered, as seen in Fig. 4. Similarly lead displays more volatile behaviour with increasing reduction potential. However, if the amount of Cl in the fuel is high (as in MSW) lead could evaporate even at lower reduction potentials forming $PbCl_2$ (g), observed in Fig. 6. As the reduction potential increases Pb (g) and PbS (g) become major constituents. The volatility of Cu is also affected by the amount of Cl. Higher amounts of Cl, as in Fig. 5 for MSW, will favor $(CuCl)_3$ (g) formation while increasing reduction potential favors slag phase formation (Cu_2S) or Cu_3As (s). For CLC and CLG, where the air and fuel reactors are separate, corrosion and fouling in the air reactor could be reduced as the elements will be concentrated in gas outlet from the fuel reactor. The latter has a significantly lower gas flow compared to that of the air reactor, which is a big advantage.

5.1. Trace element reaction paths

There are potential benefits using an oxygen carrier which could interact with some trace elements. Under fluidized bed conditions the mixing is more intense and contact between feedstock and bed material is enhanced. Interaction with ilmenite could prevent evaporation of Zn, Cu and Pb. The global thermodynamic calculations indicate that the presence of ilmenite increases the amount of copper and zinc retained in the bottom ash as ferrites. The elemental composition in Table 3 shows that both bed materials, ilmenite and sand, contain some amount of lead. The ilmenite rich bottom ash contained $PbTiO_3$ and the silica rich ash contained $PbSiO_3$ at the particle surfaces. As discussed by Dong et al. the metal matrix reaction (1) may play a significant role for the Pb-retention [31]. This is due to incorporation reactions of metals with SiO_2, which is enhanced with increasing oxygen concentration as in reaction 1. With ilmenite rich beds one important interaction channel could be with TiO_2 and the thermodynamically favorable compound $PbTiO_3$. Thermodynamic calculations also show that reaction between lead and TiO_2 is more favorable compared to SiO_2. Considering the migration of iron and ash layer formation it is possible that lead interacts with TiO_2 at the surface of the particles, but with increasing residence time becomes a part of the titanium rich core. Both bottom ash ilmenite samples which are investigated in this work contain approximately the same amount of lead. However, the high-resolution scans showed that it was difficult to observe lead on the surface of the particles in MSW-Ilmenite (1) which could suggest that it is buried beneath the top

surface. Further studies are required to investigate the influence of residence time and the distribution of these elements inside ilmenite particles.

Ilmenite particles change when undergoing continuous redox reactions. Iron will migrate towards regions with higher oxygen potential, the particle surface, forming an iron layer [70]. The iron layer could be both of homogenous and heterogenous nature. Nevertheless, this increases the availability of iron at the surface and is one important interaction channel with the ash components [70]. As shown, the iron at the surface of ilmenite interact with both zinc and copper forming the ferrites $ZnFe_2O_4$ and $CuFe_2O_4$. Thus, it is proposed that zinc and copper are incorporated in the oxygen carrier during the redox reactions. It is of interest to further understand the effects that these elements have on the bed material and its properties.

From this study it is clear that ilmenite can interact with all investigated elements and hence be obtained as mixed oxides. The implication for combustion processes using oxygen carriers could be;

- Formation of a more benign fly ash, as some heavy metals combine with the bed material, something which could be valuable if the ashes are landfilled or recycled to soils or forests.
- Corrosion or fouling on downstream heat transfer surfaces could be less.
- Enhanced fuel conversion as mixed oxides could result in new phases which could be oxygen carriers themselves.
- Opens up for the possibility of combined process for oxygen regeneration and metal extraction, i.e. Cu and Zn.

6. Conclusions

This work has investigated trace element interaction with ilmenite using a thermodynamic modelling approach and detailed experimental work using x-ray photoelectron spectroscopy (XPS). Samples from two commercial plants utilizing two different waste fuels were investigated. XPS is found to be a good complement for sample characterization of trace elements, especially since the electron microscope and x-ray diffraction cannot detect phases and elements at lower concentrations. To summarize, the following interactions between ilmenite and zinc, copper and lead have been identified:

- Lead interacts with the titanium in ilmenite forming $PbTiO_3$
- Copper and zinc interact with iron forming ferrites $CuFe_2O_4$ and $ZnFe_2O_4$

Thermodynamic calculations were used for further understanding Zn, Cu and Pb behavior mainly under OCAC conditions, but also at conditions applicable for CLC and CLG. To improve accuracy of the thermodynamic calculations, the standard FactSage databases were complemented with relevant data from additional sources. Global calculations were useful for predicting the overall behaviour of TEs under different reducing environments while the local calculations provided detailed information about the surface composition. Both calculations are important to capture the overall behaviour and surface interactions.

The results from the local thermodynamic calculations were largely in line with the characterized compounds. The calculations at higher reduction potentials show that the propensity to form gaseous species increases, something which could have implications for the CLC and CLG processes.

Acknowledgement

Appendix A. Supplementary data

Supplementary data to this article can be found online at https://doi.org/10.1016/j.biombioe.2021.106060.

References

[1] IPCC, Summary for policymakers, in: V. Masson-Delmotte, P. Zhai, H.O. Pörtner, D. Roberts, J. Skea, P.R. Shukla, et al. (Eds.), Global Warming of 1.5°C. An IPCC Special Report on the Impacts of Global Warming of 1.5°C above Pre-industrial Levels and Related Global Greenhouse Gas Emission Pathways, in the Context of Strengthening the Global Response to the Threat of Climate Change, Sustainable Development, and Efforts to Eradicate Poverty, 2018, p. 32. Geneva, Switzerland.

[2] M. Rydén, A. Lyngfelt, Langørgen Ø, Y. Larring, A. Brink, S. Teire, et al., Negative CO2 emissions with chemical-looping combustion of biomass – a nordic energy research flagship project, Energy Procedia 114 (2017) 6074–6082.

[3] On the Promotion of the Use of Energy from Renewable Sources (Recast), Directive of the European Parliament and of the Council (European Commission), 2016.

[4] IPCC, in: R. Pachauri, L. Meyer (Eds.), Climate Change 2014: Synthesis Report. Contribution of Working Groups I, II and III to the Fifth Assessment Report of the Intergovernmental Panel on Climate Change, 2014.

[5] A.A. Khan, W. de Jong, P.J. Jansens, H. S. Biomass combustion in fluidized bed boilers: potential problems and remedies, Fuel Process. Technol. 90 (2009) 21–50.

[6] A. Lyngfelt, B. Leckner, T. Mattisson, A fluidized-bed combustion process with inherent CO2 separation; application of chemical-looping combustion, Chem. Eng. Sci. 56 (2001) 3101–3113.

[7] J. Adanez, A. Abad, F. Garcia-Labiano, P. Gayan, L.F. de Diego, Progress in chemical-looping combustion and reforming technologies, Prog. Energy Combust. Sci. 38 (2012) 215–282.

[8] P. Moldenhauer, A. Gyllén, H. Thunman, F. Lind, A Scale-Up Project for Operating a 115 MWth Biomass-Fired CFB Boiler with Oxygen Carriers as Bed Material, 2018.

[9] This Is Improbed™ - Improbed. Malmö, Sweden.

[10] H. Thunman, F. Lind, C. Breitholtz, N. Berguerand, M. Seemann, Using an oxygen-carrier as bed material for combustion of biomass in a 12-MWth circulating fluidized boiler, Fuel 113 (2013) 300–309.

[11] F. Lind, A. Corcoran, B. Andersson, H. Thunman, 12,000 hours of operation with oxygen-carriers in industrially relevant scale (75,000 kWth), VGB Power Tech. (2017).

[12] Svensk Avfallshantering 2019, Avfall Sverige, 2020. Available at: https://www.avfallsverige.se.

[13] M. Vigoureux, P. Knutsson, F. Lind, Sulfur uptake during oxygen-carrier-aided combustion with ilmenite, Energy Fuel. 34 (2020) 7735–7742.

[14] A. Corcoran, J. Marinkovic, F. Lind, H. Thunman, P. Knutsson, M. Seemann, Ash properties of ilmenite used as bed material for combustion of biomass in a circulating fluidized bed boiler, Energy Fuel. 28 (2014) 7672–7679.

[15] A. Corcoran, P. Knutsson, F. Lind, H. Thunman, Mechanism for migration and layer growth of biomass ash on ilmenite used for oxygen carrier aided combustion, Energy Fuel 32 (8) (2018) 8845–8856.

[16] A.K. James, R.W. Thring, S. Helle, H.S. Ghuman, Ash management review-applications of biomass bottom ash, Energies 5 (2012) 3856–3873.

[17] S.V. Vassilev, D. Baxter, C.G. Vassileva, An overview of the behaviour of biomass during combustion: Part I. Phase-mineral transformations of organic and inorganic matter, Fuel 112 (2013) 391–449.

[18] M. Camerani, A. Somogyi, M. Drakopoulos, B. Steenari, Synchrotron radiation induced μ – X-ray fluorescence spectroscopy on municipal solid waste fly ashes, Spectrochim. Acta, Part B 56 (2001) 1355–1365.

[19] A. Nzihou, B. Stanmore, The fate of heavy metals during combustion and gasification of contaminated biomass-A brief review, J. Hazard Mater. 256 (2013) 56–66.

[20] I. Obernberger, T. Brunner, G. Bärnthaler, Chemical properties of solid biofuels—significance and impact, Biomass Bioenergy 30 (2006) 973–982.

[21] B. Strömberg, Miljö- Och Förbränningsteknik - Bränslehandboken. Värmeforsk, Värmeteknisk Forskning och Arbete: Värmeforsk, 2005.

[22] W. Ma, T. Wenga, F.J. Frandsen, B. Yan, G. Chen, The fate of chlorine during MSW incineration: vaporization, transformation, deposition, corrosion and remedies, Prog. Energy Combust. Sci. 76 (2020) 100789.

[23] A.-L. Elled, L.-E. Åmand, D. Eskilsson, Fate of zinc during combustion of demolition wood in a fluidized bed boiler, Energy Fuel. 22 (2008) 1519–1526.

[24] H. Kinnunen, M. Hedman, D. Lindberg, S. Enestam, P. Yrjas, Corrosion in recycled wood combustion—reasons, consequences, and solutions, Energy Fuel. 33 (2019) 5859–5866.

[25] J. Tang, B.-M. Steenari, Leaching optimization of municipal solid waste incineration ash for resource recovery: a case study of Cu, Zn, Pb and Cd, Waste Manag. 48 (2016) 315–322.

[26] M. Becidan, L. Sørum, D. Lindberg, Impact of municipal solid waste (MSW) quality on the behavior of alkali metals and trace elements during combustion: a thermodynamic equilibrium analysis, Energy Fuel. 24 (2010) 3446–3455.

[27] S. Enestam, R. Backman, K. Mäkelä, M. Hupa, Evaluation of the condensation behavior of lead and zinc in BFB combustion of recovered waste wood, Fuel Process. Technol. 105 (2013) 161–169.

[28] T. Talonen, Chemical Equilibria of Heavy Metals in Waste Incineration: Comparison of Thermodynamic Databases [Licentiate], Åbo Akademi University, 2008.

[29] F.J. Frandsen, K. Dam-Johansen, P. Rasmussen, Trace elements from combustion and gasification of coal—an equilibrium approach, Prog. Energy Combust. Sci. 20 (1994) 115–138.

[30] A.J. Pedersen, S.C. van Lith, F.J. Frandsen, S.D. Steinsen, L.B. Holgersen, Release to the gas phase of metals, S and Cl during combustion of dedicated waste fractions, Fuel Process. Technol. 91 (2010) 1062–1072.

[31] J. Dong, Y. Chi, Y. Tang, M. Ni, A. Nzihou, E. Weiss-Hortala, et al., Partitioning of heavy metals in municipal solid waste pyrolysis, gasification, and incineration, Energy Fuel. 29 (2015) 7516–7525.

[32] M.A. Alvin, E.P. O'Neill, L.N. Yannopoulos, D.L. Keairns, Evaluation of Trace Element Release from Fluidized-Bed Combustion Systems. Final Report, December 1975–January 1977. Westinghouse Electric Corp, in: Medium: X; Size, Research and Development Center, Pittsburgh, PA (USA), 1978, p. 102.

[33] R. Backman, M. Hupa, M. Hiltunen, K. Peltola, Interaction of the Behavior of Lead and Zinc with Alkalis in Fluidized Bed Combustion or Gasification of Waste Derived Fuels. 18th International Conference on Fluidized Bed Combustion, 2005.

[34] H. Wang, X. Dou, A. Veksha, W. Liu, A. Giannis, L. Ge, et al., Barium aluminate improved iron ore for the chemical looping combustion of syngas, Appl. Energy 272 (2020) 115236.

[35] H. Gu, L. Shen, Z. Zhong, Y. Zhou, W. Liu, X. Niu, et al., Interaction between biomass ash and iron ore oxygen carrier during chemical looping combustion, Chem. Eng. J. 277 (2015) 70–78.

[36] S. Zhang, R. Xiao, Performance of iron ore oxygen carrier modified by biomass ashes in coal-fueled chemical looping combustion, Greenh. Gases: Sci. Technol. 6 (2016) 695–709.

[37] G-q Wei, J. Feng, Y.-L. Hou, F.-Z. Li, W.-Y. Li, Z. Huang, et al., Ca-enhanced hematite oxygen carriers for chemical looping reforming of biomass pyrolyzed gas coupled with CO2 splitting, Fuel 285 (2021) 119125.

[38] A. Rubel, Y. Zhang, K. Liu, J. Neathery, Effect of ash on oxygen carriers for the application of chemical looping combustion, Oil Gas Sci. Technol. 66 (2011) 291–300.

[39] M.M. Azis, H. Leion, E. Jerndal, B.M. Steenari, T. Mattisson, A. Lyngfelt, The effect of bituminous and lignite ash on the performance of ilmenite as oxygen carrier in chemical-looping combustion, Chem. Eng. Technol. 36 (2013) 1460–1468.

[40] J. Bao, Z. Li, N. Cai, Interaction between iron-based oxygen carrier and four coal ashes during chemical looping combustion, Appl. Energy 115 (2014) 549–558.

[41] R. Siriwardane, H. Tian, G. Richards, T. Simonyi, J. Poston, Chemical-looping combustion of coal with metal oxide oxygen carriers, Energy Fuel. 23 (2009) 3885–3892.

[42] A.Y. Ilyushechkin, M. Kochanek, S. Lim, Interactions between oxygen carriers used for chemical looping combustion and ash from brown coals, Fuel Process. Technol. 147 (2016) 71–82.

[43] A. Gyllén, P. Knutsson, F. Lind, H. Thunman, Magnetic separation of ilmenite used as oxygen carrier during combustion of biomass and the effect of ash layer buildup on its activity and mechanical strength, Fuel 269 (2020) 117470.

[44] Arm M, Lindeberg J, Rodin Å, Öhrström A, Backman R, Öhman M, et al. Gasbildning i aska. In: AB VS, editor. MilILJÖRIKTIG ANVÄNDNING AV ASKOR 9572006.

[45] J.M. Moulder, W.F. Stickle, P.E. Sobol, Kd Bomben, Handbook of X-Ray Photoelectron Spectroscopy - A Reference Book of Standard Spectra for Identification and Interpretation of XPS Data. 6509 Flying Cloud Drive Eden Prairie, Minnesota 55344 United Stales of America: Perkin-Elmer Corporation - Physical Electronics Division, 1992.

[46] V.A. Naumkin, A. Kraut-Vass, S.W. Gaarenstroom, C.J. Powell, NIST X-Ray Photoelectron Spectroscopy Database - NIST Standard Reference Database 20, National Institute of Standards and Technology, Gaithersburg MD, 2012, p. 20899. Version 4. 6 June 2000.

[47] C.W. Bale, E. Bélisle, P. Chartrand, S.A. Decterov, G. Eriksson, A.E. Gheribi, et al., FactSage thermochemical software and databases - 2010 - 2016, Calphad 54 (2016) 35–53.

[48] A. Roine, HSC Chemistry® [Software], Outotec, Pori, 2018.

[49] Determination of the fossil carbon content in combustible municipal solid waste in Sweden, Avfall Sverige Utveckling Rep. U2012 2 (2012).

[50] H. Leion, A. Lyngfelt, M. Johansson, E. Jerndal, T. Mattisson, The use of ilmenite as an oxygen carrier in chemical-looping combustion, Chem. Eng. Res. Des. 86 (2008) 1017–1026.

[51] M. Humar, J. Jermer, R. Peek, Regulations in the European Union with Emphasis on Germany, Sweden and Slovenia, 2006, pp. 37–57.

[52] A.J. Pedersen, F. Flemming, C. Riber, T. Astrup, S.N. Thomsen, K. Lundtorp, et al., A full-scale study on the partitioning of trace elements in municipal solid waste incineration-effects of firing different waste types, Energy Fuel. 23 (2009) 3475, 2489.

[53] M.C. Biesinger, Advanced analysis of copper X-ray photoelectron spectra, Surf. Interface Anal. 49 (2017) 1325–1334.

[54] N.S. McIntyre, M.G. Cook, X-ray photoelectron studies on some oxides and hydroxides of cobalt, nickel, and copper, Anal. Chem. 47 (1975) 2208–2213.

[55] X. Li, A. Liu, D. Chu, C. Zhang, Y. Du, J. Huang, et al., High performance of manganese porphyrin sensitized p-type CuFe2O4 photocathode for solar water splitting to produce hydrogen in a tandem photoelectrochemical cell, Catalysts 8 (2018) 108.

[56] G. van der Laan, C. Westra, C. Haas, G.A. Sawatzky, Satellite structure in photoelectron and Auger spectra of copper dihalides, Phys. Rev. B 23 (1981) 4369–4380.

[57] L.S. Dake, D.R. Baer, J.M. Zachara, Auger parameter measurements of zinc compounds relevant to zinc transport in the environment, Surf. Interface Anal. 14 (1989) 71–75.

[58] X. Guo, H. Zhu, M. Si, C. Jiang, D. Xue, Z. Zhang, et al., ZnFe2O4 nanotubes: microstructure and magnetic properties, J. Phys. Chem. C 118 (2014) 30145–30152.

[59] S. Bera, A.A.M. Prince, S. Velmurugan, P.S. Raghavan, R. Gopalan, G. Panneerselvam, et al., Formation of zinc ferrite by solid-state reaction and its characterization by XRD and XPS, J. Mater. Sci. 36 (2001) 5379–5384.

[60] B.R. Strohmeier, D.M. Hercules, Surface spectroscopic characterization of the interaction between zinc ions and γ-alumina, J. Catal. 86 (1984) 266–279.

[61] S. Iaiche, A. Djelloul, ZnO/ZnAl2O4 nanocomposite films studied by X-Ray diffraction, FTIR, and X-Ray photoelectron spectroscopy, J. Spectrosc. (2015).

[62] L.R. Pederson, Two-dimensional chemical-state plot for lead using XPS, J. Electron. Spectrosc. Relat. Phenom. 28 (1982) 203–209.

[63] A. Cuadrat, A. Abad, J. Adánez, L.F. De Diego, F. García-Labiano, P. Gayán, Behavior of ilmenite as oxygen carrier in chemical-looping combustion, Fuel Process. Technol. 94 (2012) 101–112.

[64] P. Wang, N. Means, D. Shekhawat, D. Berry, M. Massoudi, Chemical-looping combustion and gasification of coals and oxygen carrier development: a brief review, Energies 8 (2015) 10605–10635.

[65] J. Yan, X. Lu, Q. Wang, Y. Kang, J. Li, Z. Xu, et al., Study on the influence of secondary air on the distributions of flue gas composition at the lower part of a 600 MW supercritical CFB boiler, Fuel Process. Technol. 196 (2019) 106035.

[66] J. Dai, K. Whitty, Effects of coal ash on CuO as an oxygen carrier for chemical looping with oxygen uncoupling, Energy Fuel. 32 (2018) 11656–11665.

[67] M. Durmaz, N. Dilmaç, Ö.F. Dilmaç, Evaluation of performance of copper converter slag as oxygen carrier in chemical-looping combustion (CLC), Energy 196 (2020) 117055.

[68] E. Darwish, D. Yılmaz, H. Leion, Experimental and thermodynamic study on the interaction of copper oxygen carriers and oxide compounds commonly present in ashes, Energy Fuel. 33 (2019) 2502–2515.

[69] Y.-L. Kuo, W.-C. Huang, Y.-H. Tseng, S.-H. Chang, Y. Ku, H.-Y. Lee, Electric arc furnace dust as an alternative low-cost oxygen carrier for chemical looping combustion, J. Hazard Mater. 342 (2018) 297–305.

[70] P. Knutsson, C. Linderholm, Characterization of ilmenite used as oxygen carrier in a 100 kW chemical-looping combustor for solid fuels, Appl. Energy 157 (2015) 368–373.